

Triplons, Magnons, and Spinons in a Single Quantum Spin System: SeCuO₃

Luc Testa,^{1,*} Vinko Šurija,² Krunoslav Prša,¹ Paul Steffens,³ Martin Boehm,³ Philippe Bourges,⁴ Helmuth Berger,¹ Bruce Normand,^{5,6,1} Henrik M. Rønnow,^{1,†} and Ivica Živković¹

¹*Institute of Physics, Ecole Polytechnique Fédérale de Lausanne (EPFL), CH-1015 Lausanne, Switzerland*

²*Institute of Physics, Bijenička 46, HR-10000 Zagreb, Croatia*

³*Institut Laue-Langevin, BP 156, 38042 Grenoble Cedex 9, France*

⁴*Université Paris-Saclay, CNRS, CEA, Laboratoire Léon Brillouin, 91191, Gif-sur-Yvette, France*

⁵*Paul Scherrer Institute, CH-5232 Villigen PSI, Switzerland*

⁶*Lehrstuhl für Theoretische Physik I, Technische Universität Dortmund,
Otto-Hahn-Strasse 4, 44221 Dortmund, Germany*

(Dated: January 31, 2022)

Quantum magnets display a wide variety of collective excitations, including spin waves (magnons), coherent singlet-triplet excitations (triplons), and pairs of fractional spins (spinons). These modes differ radically in nature and properties, and in all conventional analyses any given material is interpreted in terms of only one type. We report inelastic neutron scattering measurements on the spin-1/2 antiferromagnet SeCuO₃, which demonstrate that this compound exhibits all three primary types of spin excitation. Cu₁ sites form strongly bound dimers while Cu₂ sites form a network of spin chains, whose weak three-dimensional (3D) coupling induces antiferromagnetic order. We perform quantitative modeling to extract all of the relevant magnetic interactions and show that magnons of the Cu₂ system give a lower bound to the spinon continua, while the Cu₁ system hosts a band of high-energy triplons at the same time as frustrating the 3D network.

The exotic collective excitations observed in magnetic materials emerge from the rich spectrum of possible effects when quantum spin fluctuations act in different geometries, dimensionalities, and with different degrees of frustration. When fluctuations push a system beyond robust magnetic order and textbook spin waves, common types of excitation include triplons arising from structural dimerization [1–3] and frustration [4], bound states of magnons and triplons [5–8], and fractions of magnons and triplons; these latter include spinons [2, 9, 10], solitons [11, 12], Majorana quasiparticles [13–15], and other topological objects. In all these situations, the system is normally analyzed in terms of just one type of excitation, and detailed theoretical and numerical approaches have been developed for comparison with experiment.

However, an often overlooked category is the set of quantum magnets in which magnetic order is present only as a rather thin veneer on a “background” dominated by quantum fluctuations. While the Bragg peaks and magnons of the ordered spin component tend to dominate the measured experimental response, no rule states that the remaining spin fluctuations should be incoherent. The field- [16] and pressure-induced [17] quantum phase transitions of TiCuCl₃ provide an example of arbitrarily weak antiferromagnetic order superposed on a fluctuating dimer system with triplon excitations. In KCuF₃, weak coupling of the spin chains produces magnetic order superposed on a system of spinons, which is revealed at high energy [18]. Candidate spinon excitations also coexist with square-lattice antiferromagnetism [19], and many low-dimensional metal-organic systems offer the possibility of controlling this coexistence [20]. One structural route to the same phenomena is provided

by the spin-tetrahedron material Cu₂Te₂O₅X₂ (X = Cl, Br) [21], where the magnetic response is dominated by the non-ordered spins [22], a situation anticipated in theory [23], and incommensurate magnetism [24] coexists with anomalous coupled-cluster excitations [25]; similar coupled-cluster physics has been pursued in a number of other materials [26–28]. Another is the recent discovery [29] of both spinons and magnons in very weakly coupled chains of two different types.

Here we investigate the coexistence of multiple excitation types by an inelastic neutron scattering (INS) study of SeCuO₃. This compound displays both quasi-localized high-energy states and weak magnetic order at low temperatures. We demonstrate that the excitation spectrum has one triplon branch, dispersing weakly around 27 meV, and a magnon-like branch below 4 meV, whose associated scattering intensity shows the clear fingerprints of spinon continua. By model calculations using linear spin-wave theory and perturbative methods, we deduce the interaction parameters of a minimal magnetic Hamiltonian, allowing us to describe SeCuO₃ in terms of two interacting spin subsystems, namely dimers and chains, each of which shapes the magnetic excitations of the other.

The $S = 1/2$ quantum magnet SeCuO₃ [30] has a monoclinic unit cell with space group P2₁/n and lattice parameters $a = 7.71$ Å, $b = 8.24$ Å, $c = 8.50$ Å, and $\beta = 99.12^\circ$. Two crystallographically inequivalent Cu sites, Cu₁ and Cu₂, are each surrounded by six O atoms, forming CuO₄ plaquettes, with the remaining two O atoms forming the elongated octahedra represented for the Cu₂ atoms in Figs. 1(a) and 1(e). This elongation favors the $d_{x^2-y^2}$ orbitals, ensuring strong Cu₁

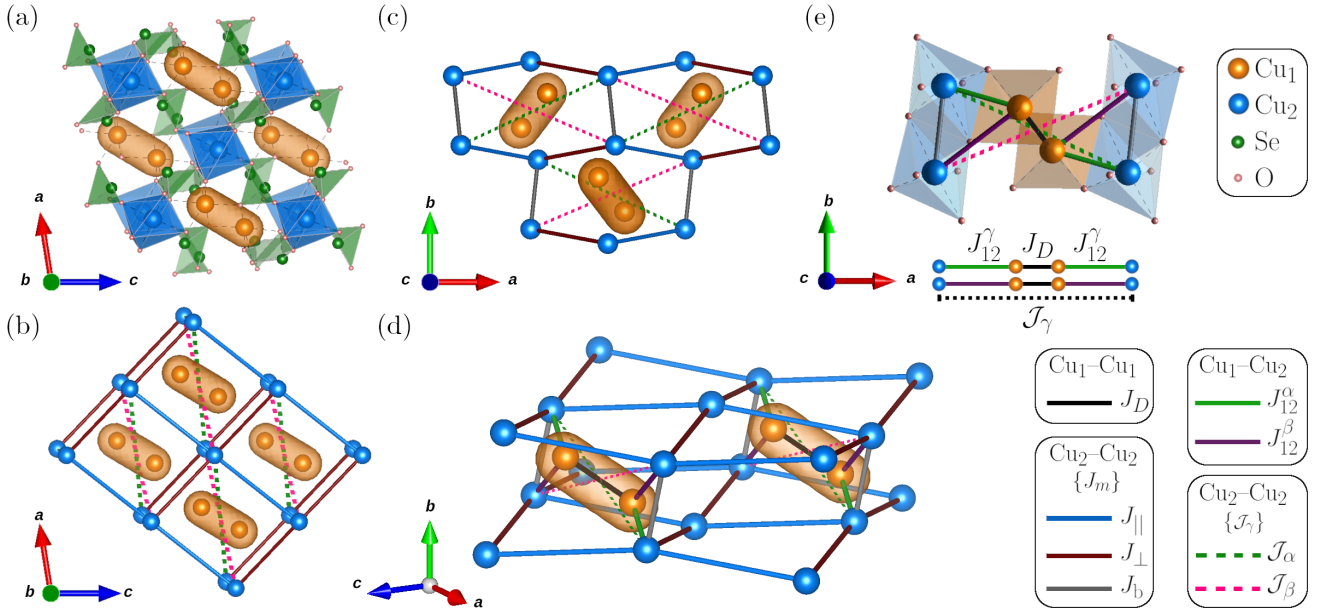


Figure 1. Atomic structure and magnetic interactions of SeCuO_3 . (a) Schematic representation of the atomic structure showing Cu_1 (orange), Cu_2 (blue), Se (green), and O (pink) atoms. (b) Projection on the ac and (c) on the ab plane, indicating the magnetic interactions of Table I. (d) Perspective view highlighting the Cu_2 chains and the direct interactions connecting them into coupled, buckled planes. (e) Geometry of the effective interactions mediated between Cu_2 atoms by the Cu_1 dimer units: \mathcal{J}_α and \mathcal{J}_β are given in terms of the two different Cu_1-Cu_2 interactions, J_{12}^α (green) and J_{12}^β (purple), and the dimer interaction, J_D (black), by Eq. (2).

dimer units (orange shading in Fig. 1) of edge-sharing plaquettes whose superexchange paths have a $\text{Cu}_1-\text{O}-\text{Cu}_1$ angle of 101.9° [31]. Including the $\text{Cu}_2 d_{x^2-y^2}$ orbitals led to the proposal of a weakly coupled network of linear ($\text{Cu}_2-\text{Cu}_1-\text{Cu}_1-\text{Cu}_2$) tetramers [31], although this scenario cannot explain the magnetic susceptibility below 90 K. Recent nuclear quadrupole resonance (NQR) measurements confirmed the formation of singlet states at $T \lesssim 200$ K [32], and together with nuclear magnetic resonance (NMR), electron spin resonance (ESR), and torque magnetometry experiments [33, 34] were interpreted as reflecting two essentially decoupled subsystems, the strong, local Cu_1 dimers and weakly coupled Cu_2 spins hosting magnetic order below $T_N = 8$ K.

To access the full spin dynamics of SeCuO_3 , we grew a 1 g single-crystal sample by chemical vapor transport. Thermal neutron INS measurements were performed on the IN8 spectrometer (ILL [35]) to probe the (hkh) scattering plane. The low-energy dynamics were studied on the cold-neutron spectrometers ThALES (ILL [36]) and 4F1 (LLB), the latter experiment probing the $(h\bar{k}\bar{h})$ scattering plane. Full details of the instrumental set-ups employed are provided in Sec. S1 of the SM [37]. The measured intensities, $I(\mathbf{q}, \omega)$, are directly proportional to the dynamical structure factor, $S(\mathbf{q}, \omega)$, for scattering processes at momentum transfer \mathbf{q} and energy transfer ω .

In Fig. 2 we present the high-energy dynamics of SeCuO_3 as measured on IN8. We obtained $I(\mathbf{q}, \omega)$ for

\mathbf{q} points along two orthogonal high-symmetry directions. At 2 K, each energy scan [Fig. 2(a)] has a resolution-limited peak that we fit with a Gaussian at all \mathbf{q} points to extract a weak dispersion around 26.5 meV [Fig. 2(b)], with smooth changes in intensity [Fig. 2(c)]. At 15 K, i.e. above T_N , the peak shows only a minimal downward shift and increased broadening [Fig. 2(a)]. Figures 2(d)-2(f) confirm that this mode persists at least until 120 K, i.e. far beyond T_N , and that its width is captured by the Lorentzian component of a Voigt line shape.

The weak \mathbf{q} -dependence of this excitation indicates its nature as a near-localized triplon of the Cu_1 dimers, whose energy is given by J_D in Fig. 1. Its Lorentzian width increases linearly with temperature until a value of 4 meV [Figs. 2(d) and 2(e)], which we will show reflects the coupling to the excitations of the Cu_2 subsystem. However, the primary thermal effect is intrinsic, as shown in Fig. 2(f) by comparing the mode amplitude with the probability, $[1 + 3 \exp(-J_D/k_B T)]^{-1}$, of finding a J_D dimer in its singlet state at temperature T , which further confirms the triplon nature of this mode.

Turning to the low-energy dynamics measured at 2 K on ThALES and 4F1, representative background-subtracted constant- \mathbf{q} ω scans are shown in Fig. 3. A strong low-energy mode is present at all \mathbf{q} , but a continuum of scattering states persists above this feature, at least up to the highest measured energy of 4.5 meV. To visualize this continuum scattering, we present our

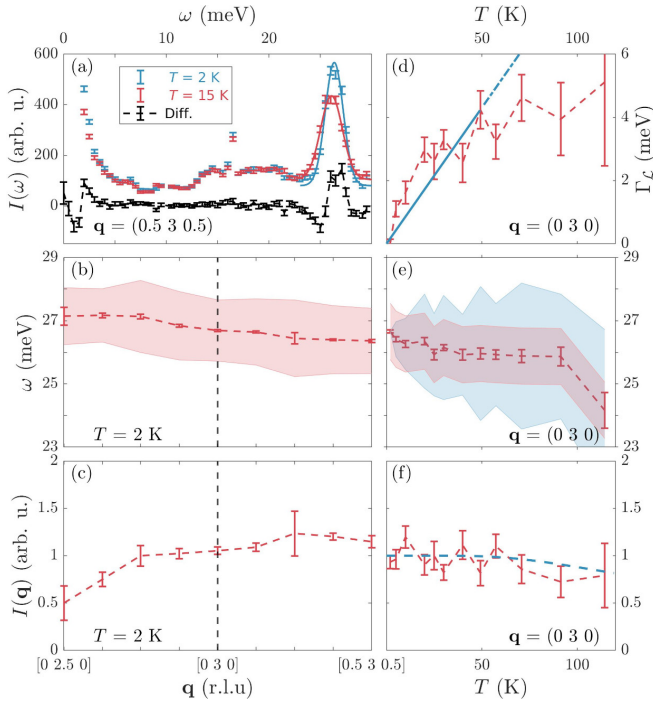


Figure 2. Triplon excitation. (a) Intensity, $I(\omega)$, at $\mathbf{q} = (0.5 \ 3 \ 0.5)$, measured at low (blue) and intermediate (red) temperatures with the difference shown in black. (b) Dispersion, $\omega(\mathbf{q})$, of the triplon in two orthogonal \mathbf{q} directions; shading represents the width (FWHM) of the mode at each \mathbf{q} point. (c) Integrated intensity, $I(\mathbf{q})$, for the same directions. (d)-(f) Thermal evolution at $\mathbf{q} = (0 \ 3 \ 0)$. (d) Lorentzian width, Γ_L (red), compared to $k_B T$ (blue). (e) $\omega(\mathbf{q}, T)$; shading indicates the instrumental resolution of 1.8(2) meV (red) and the Lorentzian profile (blue). (f) Normalized $I(\mathbf{q})$ in red compared with the thermal singlet population (blue).

intensity data as color maps in Fig. 4, and note that it appears in all three dimensions of reciprocal space. We return below to a detailed discussion of this continuum.

For a systematic analysis we perform a Gaussian fit to the peak at the lower edge of the continuum (Fig. 3) and collect two separate intensity contributions, I_p from the Gaussian and I_c from the excess scattering at all higher energies. The upper panels of Fig. 4 show the values of $I_p(\mathbf{q})$ and $I_c(\mathbf{q})$ extracted from 74 energy scans. The lower panels show a well-defined band with a maximum of 4 meV and a small gap, $\Delta = 0.42(3)$ meV, where $I_p(\mathbf{q})$ becomes large due to the magnetic order.

We expect that, with the exception of a term opening the gap, the minimal magnetic Hamiltonian contains only Heisenberg interactions between near-neighbor spins in all directions, and thus takes the form

$$\hat{\mathcal{H}} = J_D \sum_{\langle i_1, j_1 \rangle} \hat{\mathbf{S}}_{i_1} \cdot \hat{\mathbf{S}}_{j_1} + \sum_{\langle i_1, i_2 \rangle, \gamma} J_{12}^\gamma \hat{\mathbf{S}}_{i_1} \cdot \hat{\mathbf{S}}_{i_2} + \sum_{[i_2, j_2]_m} J_m \hat{\mathbf{S}}_{i_2} \cdot \hat{\mathbf{S}}_{j_2}. \quad (1)$$

Here i_1 and j_1 denote Cu_1 sites and i_2 and j_2 Cu_2 sites, $\langle \dots \rangle$ denotes a sum restricted to nearest-neighbor bonds

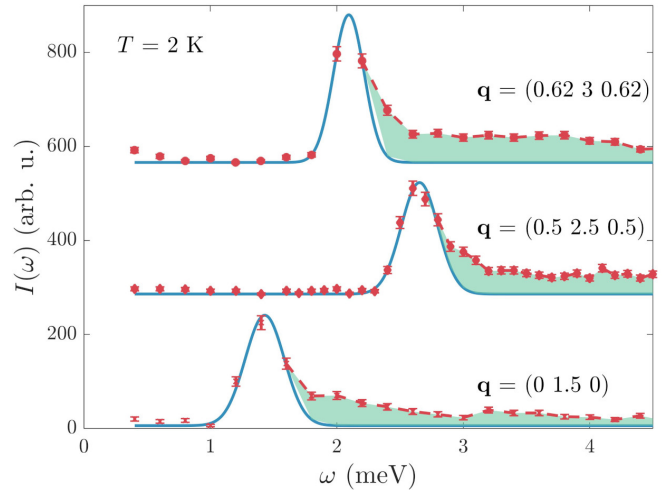


Figure 3. Magnon peak and scattering continua. $I(\omega)$ at three different \mathbf{q} points. Measured data (red points) are fitted by a Gaussian peak (blue line) at the lower edge. Green shading indicates a scattering continuum at higher energies.

and $[\dots]_m$ a sum over bonds in the set $\{J_m\}$. Having interpreted the high-energy response as a triplon of the Cu_1 subsystem with $J_D = 26.5$ meV, we build up our knowledge of the terms in Eq. (1) by next describing the low-energy response as a consequence of the decoupled Cu_2 subsystem, i.e. by neglecting the second term. For this we seek a set of interaction parameters that, used in an effective Hamiltonian of the same form as the last term of Eq. (1), reproduces the magnon dispersions and intensities in Fig. 4. As shown in Fig. 1, we allow both near-neighbor couplings, $\{J_m\}$, and long-distance “effective” couplings, $\{\mathcal{J}_\gamma\}$, over paths that include the polyhedra of other Cu_1 atoms and whose microscopic origin therefore lies in the second term of Eq. (1), as we discuss further below.

We fit $\omega(\mathbf{q})$ using linear spin-wave (LSW) theory, as implemented in the SpinW package [38], obtaining an excellent account of the INS peak positions when the interaction parameters of Fig. 1 have the values reported in Table I. This fit contains two magnon branches, one of which has over 90% of the intensity we measure. The LSW theory delivers an accurate account of $I_p(\mathbf{q})$ for the strong branch with no further fitting, as Fig. 4 makes clear, underlining its success in capturing all the leading physics of the magnon spectrum. Turning to percent-level discrepancies, in the LSW treatment the weak branch has a very low [$\mathcal{O}(0.1\%)$] intensity, whereas the intensities measured in Fig. 4 are in general 1-5% of the strong branch. While this discrepancy suggests that the magnetic Hamiltonian of SeCuO_3 contains further terms (beyond those in Table I) coupling two quasi-independent magnetic sublattices, the low intensity indicates that they are very weak.

The interactions of Table I define a Cu_2 magnetic lat-

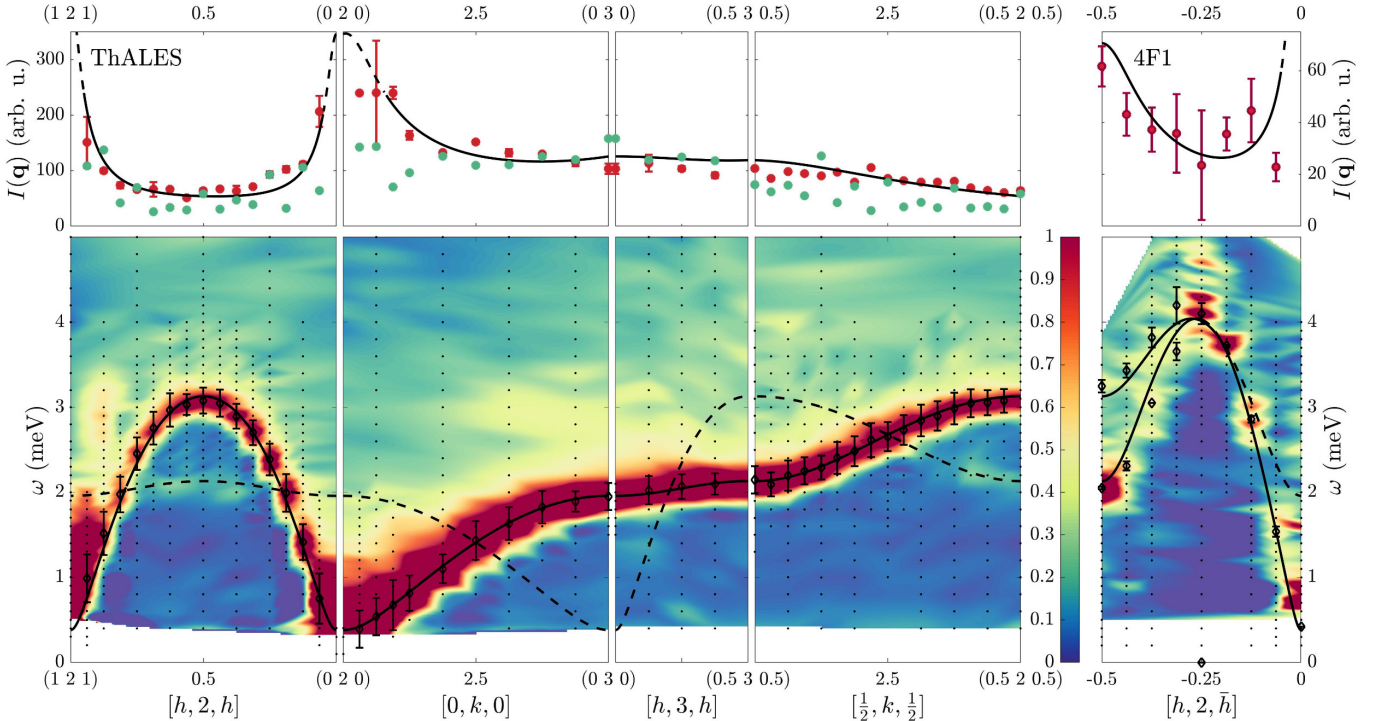


Figure 4. Magnon and spinon spectra. Colored panels show the scattering intensity, $S(\mathbf{q}, \omega)$, for five different \mathbf{q} directions. The black points show the peak centers taken from Fig. 3 and the error bars the extracted width (FWHM) of the Gaussian profiles. The black lines show the two spin-wave branches in the model fit to the lower peak of Fig. 3, one of which (dashed line) has vanishing intensity. The upper panels show the integrated intensities, $I(\mathbf{q})$, of the measured spin-wave contribution [$I_p(\mathbf{q})$, red points] and the continuum contribution [$I_c(\mathbf{q})$, green points], taken respectively from the peak and shaded areas in Fig. 3; the black lines show the spin-wave intensities given by the model parameters. In the panel at right, the intensity is a sum of two modes.

tice composed of chains aligned in the **a**–**c** direction, whose energy scale, J_{\parallel} , exceeds by a factor of 10 all the interchain couplings. From Fig. 1(a), J_{\parallel} connects Cu₂ spins through the SeO₃ tetrahedra, a superexchange path not so far considered [31–34]. This coupled-chain character provides an immediate indication for the origin of the continuum scattering in Figs. 3 and 4 as the break-up of $\Delta S = 1$ magnons into spinons at energies beyond their confinement scale. The four additional Cu₂ interactions ensure both strong interchain frustration in all three directions and the weak magnetic order at $T < T_N$. The small magnon gap can be reproduced with a tiny Ising anisotropy of J_{\parallel} , $\delta J_{\parallel} = 0.018$ meV, which has negligible

influence on the dynamics away from the zone center.

To go beyond the independent-subsystem interpretation of the excitation spectrum, we restore the coupling between Cu₁ and Cu₂ atoms in the second term of Eq. (1), without which the triplon measured in Fig. 2 would be non-dispersive. All the interactions between the Cu₂ atoms given in Table I are required to fit the dispersion data of Fig. 4 in multiple reciprocal-space directions. However, they include not only the near-neighbor couplings J_{\parallel} , J_{\perp} , and J_b , but also the couplings \mathcal{J}_{α} and \mathcal{J}_{β} whose long superexchange paths proceed directly across the Cu₁–Cu₁ dimer (Fig. 1); as a result, in a self-consistent model, these should be effective couplings arising as a consequence of J_D and of two Cu₁–Cu₂ coupling parameters, J_{12}^{γ} [Fig. 1(e)].

To estimate J_{12}^{γ} , we perform a perturbative analysis of the two four-site units shown in Fig. 1(e), as detailed in Sec. S2 of the SM [37]. The ground state in the limit $J_D \gg J_{12}^{\gamma}$, $|\Phi_0\rangle = |s_1\rangle \otimes |s_2\rangle$, is the product of two singlets on each pair of Cu₁ and Cu₂ sites. In the three lowest excited states, the Cu₁ dimer remains in a singlet while the Cu₂ spins form a triplet, $|t_2^l\rangle$, with $l = +, 0, -$. The energy difference gives the effective coupling between the

Table I. Superexchange interaction parameters within the Cu₁ and Cu₂ subsystems, in meV, obtained by fitting the dispersion data of Figs. 2(b) and 4. The geometry of the interactions is shown in Fig. 1.

Cu ₁ –Cu ₁	Cu ₂ –Cu ₂				
J_D	J_{\parallel}	J_{\perp}	J_b	\mathcal{J}_{α}	\mathcal{J}_{β}
26.5(6)	3.39(13)	0.39(3)	-0.19(2)	0.34(2)	0.35(2)

two Cu₂ atoms,

$$\mathcal{J}_\gamma = \frac{J_{12}^\gamma}{2} + \frac{1}{4} \frac{[3(J_{12}^\gamma)^2 - 2J_D J_{12}^\gamma]}{\sqrt{J_D^2 + (J_{12}^\gamma)^2}} \xrightarrow{J_D \gg J_{12}^\gamma} \frac{3}{4} \frac{(J_{12}^\gamma)^2}{J_D}. \quad (2)$$

From the fitted values of the effective couplings \mathcal{J}_α and \mathcal{J}_β (Table I), we deduce the microscopic coupling parameters to be $J_{12}^\alpha = 3.47$ meV and $J_{12}^\beta = 3.52$ meV. Our LSW fits verify that any effective coupling between atoms connected by a path involving both J_{12}^α and J_{12}^β must be vanishingly small.

Although these values are large compared to the couplings within the Cu₂ subsystem in Table I, their real effect on the spin dynamics is suppressed strongly by J_D , as the structure of Eq. (2) makes clear. Values of 3-4 meV are consistent with the width, Γ_L , of the triplon at high temperatures [Fig. 2(d)], which indicates its coupling to incoherent excitations. The perturbative treatment of Eq. (2) provides upper bounds for the J_{12}^γ values and thus is the opposite limit to the LSW approach, which cannot describe the full system of Cu₁ and Cu₂ atoms. The two approaches indicate the range of possible renormalization effects due to quantum fluctuations, which is widest at intermediate energies (corresponding to the spinon continua). The extent of renormalization to LSW theory in SeCuO₃ can be gauged from the magnetic order on the Cu₂ sublattice, which despite its 3D nature is $\mu_2 < 0.8 \mu_B$ [32]. The interactions J_{12}^γ induce order on the Cu₁ sublattice, although $\mu_1 \approx 0.35 \mu_B$ is very weak even at the lowest temperatures, and hence a full description lies well beyond the LSW approximation. The relative canting of the μ_1 and μ_2 moment directions [31] and the intensity transfer to the weak magnon branch (Fig. 4) gauge the physical effects of terms omitted in the minimal model of Eq. (1).

We return now to the most unexpected feature of our INS data, the strong continuum scattering observed directly above the magnon peaks in Figs. 3 and 4. Interpreting this as deconfined spinons requires the definitive exclusion of alternative origins. Continuum scattering above a one-magnon band arises naturally due to multi-magnon processes and has long been known in both 3D [39] and 2D antiferromagnets [40]. In this situation, the ratio of the integrated intensities, I_p in the one-magnon sector and I_c in the putative multi-magnon sector (Fig. 4), cannot exceed a well-defined limit. In Table II we average both quantities along four \mathbf{q} directions, and note further that our measured energy range may not capture the upper edge of the continuum (Fig. 3), whence the ratio $\kappa_{\min} = I_c/I_p$ constitutes a lower bound.

We find that I_c is of the same order as I_p , making their ratio far greater than those found in multimagnon scattering studies [39, 40]. The LSW prediction for this ratio can be deduced from the spin reduction (quantum fluctuation renormalization) measured [32] on the Cu₂ sublattice, and as Table II makes clear the data exclude

any straightforward multimagnon origin. We comment that highly unconventional multimagnon processes, such as those involving very strong magnon-magnon interactions, are hard to rule out, but that there is little evidence for these (such as decay of our observed magnons) in SeCuO₃. Further, the gap in the one-magnon spectrum implies a gap between the one- and multi-magnon contributions, as encountered in Ref. [40], whereas Figs. 3 and 4 exclude such a gap with even a fraction the size of the measured Δ .

Thus we conclude that the most plausible origin for the observed continuum scattering is spinons. More specifically, the strong quantum corrections of the chain-like $S = 1/2$ Cu₂ system do permit a deconfinement of spinons at energies above the one-magnon band. However, the frustrating interchain interactions, which allow this spinonic character in a system with magnetic order, mean that the resulting continua (Fig. 4) are far from the familiar single-chain form, which was found in Ref. [29] for magnons and spinons coexisting in the quasi-1D limit. The problem of partially confined spinons has recently received considerable attention in some of the paradigm Heisenberg models within frustrated quantum magnetism [41–45], and SeCuO₃ presents a materials example of this complex situation. While a detailed analysis lies beyond the scope of the present study, the locations of continuum scattering in Fig. 4 and the intensity ratios for magnon and spinon contributions will provide essential input for a complete theoretical description.

To conclude, we have investigated a member of the class of coupled-cluster, multi-subsystem quantum magnetic materials in which magnon, triplon, and spinon excitations are present simultaneously. In SeCuO₃, the clusters are strong Cu₁ dimers and the second sublattice, Cu₂, is a network of spin chains on which weak magnetic order appears below $T_N = 8$ K. By neutron spectroscopy we have determined not only the intra-sublattice interactions but also the Cu₁-Cu₂ interactions that make the Cu₁ triplon mode weakly dispersive, induce small Cu₁ moments, and create frustrating interactions in the Cu₂ sublattice, which contribute to the emergence of spinon continua above the magnons. From our results,

Table II. Integrated peak intensity, I_p , and continuum intensity, I_c , averaged along four high-symmetry directions. The lower row presents the LSW theoretical result for the spin reduction, $\Delta S_2 = 0.13$, measured [32] on the Cu₂ sublattice.

Direction	I_p	I_c	κ_{\min}
[$h, 2, h$]	90(4)	61	0.69(4)
[$0, k, 0$]	133(5)	99	0.85(4)
[$h, 3, h$]	98(4)	125	1.28(4)
[$\frac{1}{2}, k, \frac{1}{2}$]	85(4)	56	0.65(4)
$\Delta S_2 = 0.13$	0.47	0.15	0.32

SeCuO3 encapsulates the challenge of describing the coherent quantum correlations, or quantum entanglement, that in many systems lie beneath the (unentangled) veneer of magnetic order, and mandates an integrated theoretical treatment of how these correlations lead to all three coexisting excitation types.

Acknowledgments. We thank X. Rocquefelte for helpful discussions. We are grateful to the Swiss National Science Foundation (SNSF) for financial support under Grant No. 188648 and the European Research Council (ERC) for the support of the Synergy Grant HERO. Research at TU Dortmund was supported by the Deutsche Forschungsgemeinschaft (DFG, German Research Foundation) through Grants No. UH90/13-1 and UH90/14-1. We thank the Institut Laue-Langevin and the Laboratoire Léon Brillouin for access to their neutron scattering facilities. These neutron scattering experiments were performed within the framework of the EUROfusion Consortium, which was funded by the Euratom Research and Training Programme 2014–2018 under Grant Agreement No. 633053.

* luc.testa@gmail.com

† henrik.rønnow@epfl.ch

- [1] N. Cavadini, G. Heigold, W. Henggeler, A. Furrer, H.-U. Güdel, K. Krämer, and H. Mutka, “Magnetic excitations in the quantum spin system TiCuCl3,” *Phys. Rev. B* **63**, 172414 (2001).
- [2] B. Thielemann, C. Rüegg, H. M. Rønnow, A. M. Läuchli, J.-S. Caux, B. Normand, D. Biner, K. W. Krämer, H.-U. Güdel, J. Stahn, K. Habicht, K. Kiefer, M. Boehm, D. F. McMorrow, and J. Mesot, “Direct Observation of Magnon Fractionalization in the Quantum Spin Ladder,” *Phys. Rev. Lett.* **102**, 107204 (2009).
- [3] D. Schmidiger, S. Mühlbauer, A. Zheludev, P. Bouillot, T. Giamarchi, C. Kollath, G. Ehlers, and A. M. Tsvelik, “Symmetric and asymmetric excitations of a strong-leg quantum spin ladder,” *Phys. Rev. B* **88**, 094411 (2013).
- [4] B. D. Gaulin, S. H. Lee, S. Haravifard, J. P. Castellan, A. J. Berlinsky, H. A. Dabkowska, Y. Qiu, and J. R. D. Copley, “High-Resolution Study of Spin Excitations in the Singlet Ground State of SrCu2(BO3)2,” *Phys. Rev. Lett.* **93**, 267202 (2004).
- [5] J. B. Torrance and M. Tinkham, “Excitation of Multiple-Magnon Bound States in CoCl2·2H2O,” *Phys. Rev.* **187**, 595–606 (1969).
- [6] G. S. Uhrig and H. J. Schulz, “Magnetic excitation spectrum of dimerized antiferromagnetic chains,” *Phys. Rev. B* **54**, R9624–R9627 (1996).
- [7] S. Ward, M. Mena, P. Bouillot, C. Kollath, T. Giamarchi, K. P. Schmidt, B. Normand, K. W. Krämer, D. Biner, R. Bewley, T. Guidi, M. Boehm, D. F. McMorrow, and C. Rüegg, “Bound States and Field-Polarized Haldane Modes in a Quantum Spin Ladder,” *Phys. Rev. Lett.* **118**, 177202 (2017).
- [8] P. A. McClarty, F. Krüger, T. Guidi, S. F. Parker, K. Refson, A. W. Parker, D. Prabhakaran, and R. Coldea, “Topological triplon modes and bound states in a Shastry–Sutherland magnet,” *Nat. Phys.* **13**, 736–741 (2017).
- [9] P. R. Hammar, M. B. Stone, D. H. Reich, C. Broholm, P. J. Gibson, M. M. Turnbull, C. P. Landee, and M. Oslikawa, “Characterization of a quasi-one-dimensional spin-1/2 magnet which is gapless and paramagnetic for $g\mu_B H \lesssim J$ and $k_B T \ll J$,” *Phys. Rev. B* **59**, 1008–1015 (1999).
- [10] M. Mourigal, M. Enderle, A. Klöpperpieper, J.-S. Caux, A. Stunault, and H. M. Rønnow, “Fractional spinon excitations in the quantum Heisenberg antiferromagnetic chain,” *Nat. Phys.* **9**, 435–441 (2013).
- [11] S. E. Nagler, W. J. L. Buyers, R. L. Armstrong, and B. Briat, “Solitons in the one-dimensional antiferromagnet CsCoBr3,” *Phys. Rev. B* **28**, 3873–3885 (1983).
- [12] Q. Faure, S. Takayoshi, S. Petit, V. Simonet, S. Raymond, L.-P. Regnault, M. Boehm, J. S. White, M. Måsson, C. Rüegg, P. Lejay, B. Canals, T. Lorenz, S. C. Furuya, T. Giamarchi, and B. Grenier, “Topological quantum phase transition in the Ising-like antiferromagnetic spin chain BaCo2V2O8,” *Nat. Phys.* **14**, 716–722 (2018).
- [13] A. Kitaev, “Anyons in an exactly solved model and beyond,” *Ann. Phys.* **321**, 2–111 (2006).
- [14] J. Chaloupka, G. Jackeli, and G. Khaliullin, “Kitaev–Heisenberg Model on a Honeycomb Lattice: Possible Exotic Phases in Iridium Oxides A2IrO3,” *Phys. Rev. Lett.* **105**, 027204 (2010).
- [15] J. Wang, B. Normand, and Z.-X. Liu, “One Proximate Kitaev Spin Liquid in the K - J - Γ Model on the Honeycomb Lattice,” *Phys. Rev. Lett.* **123**, 197201 (2019).
- [16] C. Rüegg, N. Cavadini, A. Furrer, H.-U. Güdel, K. Krämer, H. Mutka, A. Wildes, K. Habicht, and P. Vorderwisch, “Bose–Einstein condensation of the triplet states in the magnetic insulator TiCuCl3,” *Nature* **423**, 62–65 (2003).
- [17] C. Rüegg, B. Normand, M. Matsumoto, A. Furrer, D. F. McMorrow, K. W. Krämer, H. U. Güdel, S. N. Gvasaliya, H. Mutka, and M. Boehm, “Quantum Magnets under Pressure: Controlling Elementary Excitations in TiCuCl3,” *Phys. Rev. Lett.* **100**, 205701 (2008).
- [18] B. Lake, D. A. Tennant, C. D. Frost, and S. E. Nagler, “Quantum criticality and universal scaling of a quantum antiferromagnet,” *Nat. Mater.* **4**, 329–334 (2005).
- [19] B. Dalla Piazza, M. Mourigal, N. B. Christensen, G. J. Nilsen, P. Tregenna-Piggott, T. G. Perring, M. Enderle, D. F. McMorrow, D. A. Ivanov, and H. M. Rønnow, “Fractional excitations in the square-lattice quantum antiferromagnet,” *Nat. Phys.* **11**, 62–68 (2015).
- [20] M. Skoulatos, M. Måsson, C. Fiolka, K. W. Krämer, J. Schefer, J. S. White, and C. Rüegg, “Dimensional reduction by pressure in the magnetic framework material CuF2(D2O)2(pyz): From spin-wave to spinon excitations,” *Phys. Rev. B* **96**, 020414 (2017).
- [21] M. Johnsson, K. W. Törnroos, F. Mila, and P. Millet, “Tetrahedral Clusters of Copper(II): Crystal Structures and Magnetic Properties of Cu2Te2O5X2 ($X = Cl, Br$)”, *Chem. Mater.* **12**, 2853–2857 (2000).
- [22] Z. Jagličić, S. El Shawish, A. Jeromen, A. Bilušić, A. Smontara, Z. Trontelj, J. Bonča, J. Dolinšek, and H. Berger, “Magnetic ordering and ergodicity of the spin system in the Cu2Te2O5X2 family of quantum magnets,” *Phys. Rev. B* **73**, 214408 (2006).

- [23] V. N. Kotov, M. E. Zhitomirsky, M. Elhajal, and F. Mila, “Weak antiferromagnetism and dimer order in quantum systems of coupled tetrahedra,” *Phys. Rev. B* **70**, 214401 (2004).
- [24] O. Zaharko, A. Daoud-Aladine, S. Streule, J. Mesot, P.-J. Brown, and H. Berger, “Incommensurate Magnetic Ordering in $\text{Cu}_2\text{Te}_2\text{O}_5X_2$ ($X = \text{Cl}, \text{Br}$) Studied by Neutron Diffraction,” *Phys. Rev. Lett.* **93**, 217206 (2004).
- [25] K. Prša, H. M. Rønnow, O. Zaharko, N. B. Christensen, J. Jensen, J. Chang, S. Streule, M. Jiménez-Ruiz, H. Berger, M. Prester, and J. Mesot, “Anomalous Magnetic Excitations of Cooperative Tetrahedral Spin Clusters,” *Phys. Rev. Lett.* **102**, 177202 (2009).
- [26] R. Becker, M. Johnsson, R. K. Kremer, and P. Lemmens, “Crystal structure and magnetic properties of $\text{Cu}_3(\text{TeO}_3)_2\text{Br}_2$ – a layered compound with a new Cu(II) coordination polyhedron,” *J. Solid State Chem.* **178**, 2024–2029 (2005).
- [27] O. Zaharko, J. Mesot, L. A. Salguero, R. Valentí, M. Zbiri, M. Johnson, Y. Filinchuk, B. Klemke, K. Kiefer, M. Mys’kiv, T. Strässle, and H. Mutka, “Tetrahedra system $\text{Cu}_4\text{OCl}_6\text{daca}_4$: High-temperature manifold of molecular configurations governing low-temperature properties,” *Phys. Rev. B* **77**, 224408 (2008).
- [28] K.-Y. Choi, S. Do, P. Lemmens, J. van Tol, J. Shin, G. S. Jeon, Y. Skourski, J.-S. Rhyee, and H. Berger, “Coexistence of localized and collective magnetism in the coupled-spin-tetrahedra system $\text{Cu}_4\text{Te}_5\text{O}_{12}\text{Cl}_4$,” *Phys. Rev. B* **90**, 184402 (2014).
- [29] H. Zhang, Z. Zhao, D. Gautreau, M. Raczkowski, A. Saha, V. Garlea, H. Cao, T. Hong, H. Jeschke, S. Makhanti, T. Birol, F. Assaad, and X. Ke, “Coexistence and Interaction of Spinons and Magnons in an Antiferromagnet with Alternating Antiferromagnetic and Ferromagnetic Quantum Spin Chains,” *Phys. Rev. Lett.* **125**, 037204 (2020).
- [30] H. Effenberger, “Die Kristallstrukturen von drei Modifikationen des $\text{Cu}(\text{SeO}_3)$,” *Z. Krist.* **175**, 61–72 (1986).
- [31] I. Živković, D. M. Djokić, M. Herak, D. Pajić, K. Prša, P. Pattison, D. Dominko, Z. Micković, D. Cinčić, L. Forró, H. Berger, and H. M. Rønnow, “Site-selective quantum correlations revealed by magnetic anisotropy in the tetramer system SeCuO_3 ,” *Phys. Rev. B* **86**, 054405 (2012).
- [32] T. Cvitanić, V. Šurija, K. Prša, O. Zaharko, I. Kupčić, P. Babkevich, M. Frontzek, M. Požek, H. Berger, A. Magrez, H. M. Rønnow, M. S. Grbić, and I. Živković, “Singlet state formation and its impact on the magnetic structure in the tetramer system SeCuO_3 ,” *Phys. Rev. B* **98**, 054409 (2018).
- [33] S. Lee, W.-J. Lee, J. van Tol, P. L. Kuhns, A. P. Reyes, H. Berger, and K.-Y. Choi, “Anomalous spin dynamics in the coupled spin tetramer system CuSeO_3 ,” *Phys. Rev. B* **95**, 054405 (2017).
- [34] N. Novosel, W. Lafargue-Dit-Hauret, Z. Rapljenović, M. Dragičević, H. Berger, D. Cinčić, X. Rocquefelte, and M. Herak, “Strong decoupling between magnetic subsystems in the low-dimensional spin- $\frac{1}{2}$ antiferromagnet SeCuO_3 ,” *Phys. Rev. B* **99**, 014434 (2019).
- [35] V. Šurija, K. Prša, H. M. Rønnow, M. Boehm, and I. Živković, “ SeCuO_3 : a coupled cluster system close to criticality,” (2013), doi:10.5291/ILL-DATA.4-01-1295.
- [36] V. Šurija, K. Prša, H. M. Rønnow, P. Steffens, and I. Živković, “Low-energy magnetic modes in SeCuO_3 ,” (2015), doi:10.5291/ILL-DATA.4-01-1459.
- [37] Details are provided in the Supplemental Material at the end of this document.
- [38] S. Toth and B. Lake, “Linear spin wave theory for single-Q incommensurate magnetic structures,” *J. Phys. Condens. Matter* **27**, 166002 (2015).
- [39] R. A. Cowley, W. J. L. Buyers, P. Martel, and R. W. H. Stevenson, “Two-Magnon Scattering of Neutrons,” *Phys. Rev. Lett.* **23**, 86–89 (1969).
- [40] T. Huberman, R. Coldea, R. A. Cowley, D. A. Tennant, R. L. Leheny, R. J. Christianson, and C. D. Frost, “Two-magnon excitations observed by neutron scattering in the two-dimensional spin- $\frac{5}{2}$ Heisenberg antiferromagnet Rb_2MnF_4 ,” *Phys. Rev. B* **72**, 014413 (2005).
- [41] A. Mezio, C. N. Sposetti, L. O. Manuel, and A. E. Trumper, “A test of the bosonic spinon theory for the triangular antiferromagnet spectrum,” *Europhys. Lett.* **94**, 47001 (2011).
- [42] H. Shao, Y. Q. Qin, S. Capponi, S. Chesi, Z. Y. Meng, and A. W. Sandvik, “Nearly Deconfined Spinon Excitations in the Square-Lattice Spin-1/2 Heisenberg Antiferromagnet,” *Phys. Rev. X* **7**, 041072 (2017).
- [43] S.-L. Yu, W. Wang, Z.-Y. Dong, Z.-J. Yao, and J.-X. Li, “Deconfinement of spinons in frustrated spin systems: Spectral perspective,” *Phys. Rev. B* **98**, 134410 (2018).
- [44] E. A. Ghioldi, M. G. Gonzalez, S.-S. Zhang, Y. Kamiya, L. O. Manuel, A. E. Trumper, and C. D. Batista, “Dynamical structure factor of the triangular antiferromagnet: Schwinger boson theory beyond mean field,” *Phys. Rev. B* **98**, 184403 (2018).
- [45] F. Ferrari and F. Becca, “Dynamical Structure Factor of the J_1 - J_2 Heisenberg Model on the Triangular Lattice: Magnons, Spinons, and Gauge Fields,” *Phys. Rev. X* **9**, 031026 (2019).

Supplemental Material for “Triplons, Magnons, and Spinons in a Single Quantum Spin System: SeCuO₃”

L. Testa, V. Šurija, K. Prša, P. Steffens, M. Boehm, P. Bourges,
H. Berger, B. Normand, H. M. Rønnow, and I. Živković

S1. Experimental Details

The sample was mounted on an Al holder, using Laue x-ray backscattering to orient it in the (hkh) scattering plane. Thermal neutron measurements on IN8 used an incident neutron wave vector of 2.66 \AA^{-1} and the energy resolution at $\omega = 27 \text{ meV}$ was $1.8(2) \text{ meV}$ (FWHM). In the cold neutron measurements on ThALES and 4F1, the incident neutron wave vector was 1.55 \AA^{-1} and the resolution at $\omega = 5 \text{ meV}$ was $0.19(5) \text{ meV}$ in both cases; both experiments used a PG(002) monochromator and analyzer, and a Be filter placed after the sample to remove higher-order scattering processes. The crystal was reoriented in the $(hk\bar{h})$ scattering plane for the 4F1 experiment. Counting times in the ThALES experiment were 5 minutes per \mathbf{q} -point and on 4F1 3 minutes per point (Figs. 3 and 4 of the main text). On IN8, each \mathbf{q} -point at temperatures below and directly above the ordering transition was measured for 4 minutes [Figs. 2(a-c)], whereas one measurement during the studies of temperature-dependence lasted for 30 s [Figs. 2(d-f)]. The measured intensities, $I(\mathbf{q}, \omega)$, can be regarded as $S(\mathbf{q}, \omega)$ integrated over the resolution functions of each instrument.

S2. Four-site model

Each of the two different four-spin systems represented in Fig. 1(e) of the main text has the Heisenberg Hamiltonian

$$\hat{\mathcal{H}}_t = J_{12}^\gamma (\hat{\mathbf{S}}_{12} \cdot \hat{\mathbf{S}}_{21} + \hat{\mathbf{S}}_{31} \cdot \hat{\mathbf{S}}_{42}) + J_D \hat{\mathbf{S}}_{21} \cdot \hat{\mathbf{S}}_{31}. \quad (\text{S1})$$

The ground-state and lowest-lying excited energies obtained by diagonalization in the 16×16 Hilbert space are

$$E_0 = \frac{1}{4} \left(-J_D - 2J_{12}^\gamma - 2\sqrt{J_D^2 - 2J_D J_{12}^\gamma + 4(J_{12}^\gamma)^2} \right), \quad E_1 = \frac{1}{4} \left(-J_D - 2\sqrt{J_D^2 + (J_{12}^\gamma)^2} \right), \quad (\text{S2})$$

with corresponding eigenstates

$$\begin{aligned} |\Phi_0\rangle &= |\uparrow\uparrow\downarrow\downarrow\rangle - A|\uparrow\uparrow\downarrow\downarrow\rangle + B|\uparrow\downarrow\uparrow\downarrow\rangle + B|\downarrow\uparrow\uparrow\downarrow\rangle - A|\downarrow\uparrow\downarrow\uparrow\rangle + |\downarrow\downarrow\uparrow\uparrow\rangle, \\ |\Phi_1^-\rangle &= -|\uparrow\downarrow\downarrow\downarrow\rangle + C|\downarrow\uparrow\downarrow\downarrow\rangle - C|\downarrow\downarrow\uparrow\downarrow\rangle + |\downarrow\downarrow\uparrow\uparrow\rangle, \\ |\Phi_1^0\rangle &= -|\uparrow\uparrow\downarrow\downarrow\rangle + D|\uparrow\downarrow\uparrow\downarrow\rangle - D|\downarrow\uparrow\downarrow\uparrow\rangle + |\downarrow\downarrow\uparrow\uparrow\rangle, \\ |\Phi_1^+\rangle &= -|\uparrow\uparrow\uparrow\downarrow\rangle + C|\uparrow\uparrow\downarrow\uparrow\rangle - C|\uparrow\downarrow\uparrow\uparrow\rangle + |\downarrow\uparrow\uparrow\uparrow\rangle, \end{aligned} \quad (\text{S3})$$

in which the coefficients are given by

$$\begin{aligned} A &= \frac{2J_{12}^\gamma + \sqrt{J_D^2 - 2J_D J_{12}^\gamma + 4(J_{12}^\gamma)^2}}{J_D}, & C &= \frac{J_D + \sqrt{J_D^2 + (J_{12}^\gamma)^2}}{J_{12}^\gamma}, \\ B &= \frac{2J_{12}^\gamma (2J_{12}^\gamma + \sqrt{J_D^2 - 2J_D J_{12}^\gamma + 4(J_{12}^\gamma)^2})}{J_D (J_D + \sqrt{J_D^2 - 2J_D J_{12}^\gamma + 4(J_{12}^\gamma)^2})}, & D &= \frac{J_{12}^\gamma + \sqrt{J_D^2 + (J_{12}^\gamma)^2}}{J_D}. \end{aligned} \quad (\text{S4})$$

In the limit of strong coupling on the Cu₁ dimer ($J_D \gg J_{12}^\gamma$), it is easy to see that $A, D \rightarrow 1$, $B \rightarrow 0$, and $C \gg 1$. The eigenstates may then be reexpressed as

$$\begin{aligned} |\Phi_0\rangle &= |\uparrow\uparrow\downarrow\downarrow\rangle - |\uparrow\downarrow\downarrow\downarrow\rangle + |\downarrow\downarrow\uparrow\uparrow\rangle - |\downarrow\uparrow\downarrow\uparrow\rangle = |s_1\rangle \otimes |s_2\rangle, \\ |\Phi_1^-\rangle &= |\downarrow\downarrow\uparrow\uparrow\rangle - |\uparrow\downarrow\downarrow\downarrow\rangle + C(|\downarrow\uparrow\downarrow\downarrow\rangle - |\downarrow\downarrow\uparrow\downarrow\rangle) = C|s_1\rangle \otimes |t_2^-\rangle - |s_2\rangle \otimes |t_1^-\rangle, \\ |\Phi_1^0\rangle &= |\uparrow\downarrow\uparrow\downarrow\rangle - |\uparrow\uparrow\downarrow\downarrow\rangle + |\downarrow\downarrow\uparrow\uparrow\rangle - |\downarrow\uparrow\downarrow\uparrow\rangle = -|s_1\rangle \otimes |t_2^0\rangle, \\ |\Phi_1^+\rangle &= |\downarrow\uparrow\uparrow\uparrow\rangle - |\uparrow\uparrow\uparrow\downarrow\rangle + C(|\uparrow\uparrow\downarrow\uparrow\rangle - |\uparrow\downarrow\uparrow\uparrow\rangle) = C|s_1\rangle \otimes |t_2^+\rangle - |t_1^+\rangle \otimes |s_2\rangle, \end{aligned} \quad (\text{S5})$$

where on the right side we have introduced a singlet-triplet notation. Thus we use the energy difference, $E_1 - E_0$ in Eq. (S2), to deduce Eq. (2) of the main text and we use Eq. (S5) to demonstrate that, as a singlet-triplet energy separation on the two Cu₂ sites, it corresponds in the limit of strong J_D to an effective magnetic interaction between these sites.